Numerical Analysis of Dielectric-Rod Waveguides With Deep Corrugation

Hiroshi Kubo, *Member, IEEE*, and Masayoshi Tahara

***Abstract*—Dielectric-rod waveguides with deep surface corrugation is analyzed by using the finite-difference time-domain method. In order to mitigate the load in numerical calculation and to analyze a wide region, the method is formulated in two-dimensional form. It is shown that disks located in a line function as a waveguide of low loss in a frequency region. The procedure of deciding the propagation constant from the analyzed field is presented. The complex propagation constant is obtained and the dependence of the amount of radiation on the corrugation amplitude is discussed.**

***Index Terms*—Dielectric waveguide, discrete Fourier transforms, FDTD methods, periodic structures, propagation.**

I. Introduction

THE dielectric waveguides with a corrugated surface have been of considerable interest in the optical or millimeter-wave regions because of the important role they play in applications such as filters [1], grating couplers [2], and leaky-wave antennas [3]. There have been various studies dealing with the properties of the electromagnetic fields supported by the planar and strip dielectric waveguides with a periodic surface [4]–[7], while there exist some studies that consider cylindrical dielectric waveguides with a periodic surface. Marcuse and Derosier [8] have first analyzed the characteristics of mode conversion and radiation of guided waves in the cylindrical dielectric waveguide with a periodic boundary perturbation. Wlodarczyk and Seshadri [9] have reported a systematic analysis on the excitation and scattering of guided waves on the periodic cylindrical waveguide using a singular perturbation approach. With respect to the numerical analysis of the periodic cylindrical waveguide, there have been a few approaches. Applying the null-field method, Lundqvist [10] has pointed out several interesting features of the stopband of the guided wave. Making use of the mode-matching method, Yasumoto and Kubo [11] have discussed the convergence and accuracy of the numerical solution. In these methods, the fields are expanded in the form of a finite series of wave functions, and the results can be obtained for shallow corrugations.

In a deep corrugation, the modulation indexes are so large that the phenomena proper to periodic structure may occur intensely. In this paper, the finite-difference time-domain (FDTD) method is applied to the analyses of dielectric waveguides with deep corrugation. The disks located in a line, which can be considered an ultimate shape of corrugated rod, are also analyzed. Taking account of the field distribution of the guided wave, the FDTD method is formulated in two-dimensional form, so that longer waveguides can be calculated. It can be expected that the accuracy of the propagation constant improves by processing analysis data of a longer region. A procedure based on the discrete Fourier transformation (DFT) is presented for determining the phase constant from the FDTD results. The propagation loss is examined about the disks connected to uniform rod waveguides through transducers. The dispersion relation of the complex propagation constant is obtained for the fundamental HE_{11}-type wave. The dependence of radiative leakage on the amplitude of corrugation is brought out.

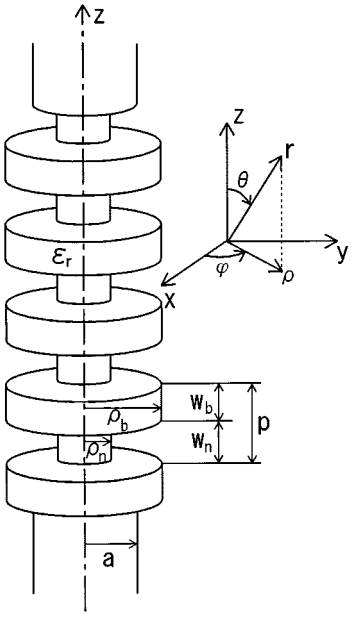

Fig. 1. Dielectric-rod waveguide with periodic structure.

II. Formulation

Fig. 1 shows a dielectric-rod waveguide with periodic structure. The surface varies rectangularly with respect to the z-direction. Shape of the corrugation is specified by w_b, w_n, ρ_b, and ρ_n and the period is denoted by p. Uniform rod waveguides with radius a are connected at both ends. We formulate the differential equations of the FDTD method in the cylindrical coordinate system for this problem. Fig. 2(a) shows the spatial relationship of the field components for an off-z-axis unit cell. Fig. 2(b)

Manuscript received March 30, 2000; revised December 6, 2000.

H. Kubo is with the Department of Electrical and Electronic Engineering, Yamaguchi University, Tokiwadai, Ube-shi 755, Japan.

M. Tahara is with the Japan Radio Company, Tokyo 107, Japan.

Publisher Item Identifier S 0018-9480(02)04068-1.

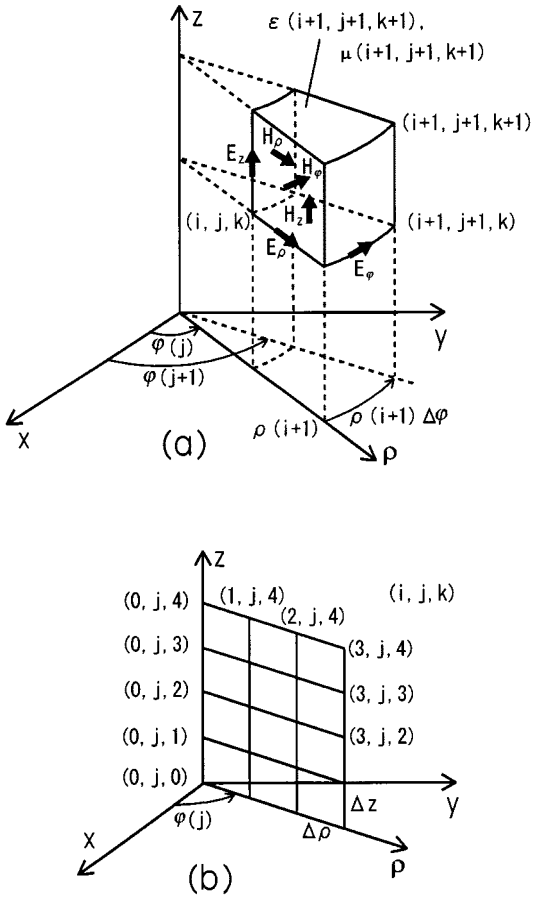

Fig. 2. (a) Spatial relationship of field components for an off-z-axis unit cell. (b) Space points in a lattice of $\varphi = \varphi(j)$.

shows the space points in a lattice of $\varphi = \varphi(j)$. The space point is denoted as (i, j, k) corresponding to the coordinates

$$(i\Delta\rho,\, j\Delta\varphi,\, k\Delta z) \tag{1}$$

where i, j, and k are natural numbers, $\Delta\rho$ and Δz are the lattice space increments in the ρ- and z-directions, and $\Delta\varphi$ is the lattice angle increment in the φ-direction. The permittivity and permeability in the cell are given by $\varepsilon(i+1,\, j+1,\, k+1)$ and $\mu(i+1,\, j+1,\, k+1)$.

Here, HE_{11}-type wave polarized in the $\varphi = \pi/2$ direction is fed through a uniform waveguide into the periodic waveguide. Since the incident wave field varies sinusoidally with respect to the φ-direction and the structure of Fig. 1 is axially symmetric, the fields in the waveguide also vary sinusoidally. Thus, the fields at the space point or the point 1/2 increment apart from it are given in the form of

$$\begin{aligned}
E_\rho &= e_\rho(i+1/2,\, k)\sin\varphi(j)\\
E_\varphi &= e_\varphi(i,\, k)\cos\varphi(j+1/2)\\
E_z &= e_z(i,\, k+1/2)\sin\varphi(j)\\
H_\rho &= h_\rho(i,\, k+1/2)\cos\varphi(j+1/2)\\
H_\varphi &= h_\varphi(i+1/2,\, k+1/2)\sin\varphi(j)\\
H_z &= h_z(i+1/2,\, k)\cos\varphi(j+1/2).
\end{aligned} \tag{2}$$

Applying Faraday's Law on the $\varphi - z$ face of the cell, the equation for computing the h_r is derived. The line integral of electric field along the four sides is approximately given by

$$\begin{aligned}
\oint E\,dl &\simeq e_z\left(i, k+\frac{1}{2}\right)\left\{\sin\varphi(j+1)-\sin\varphi(j)\right\}\Delta z\\
&\quad+\int_{\varphi(j)}^{\varphi(j+1)}\left\{e_\varphi(i,\, k)-e_\varphi(i,\, k+1)\right\}\cos\varphi\rho(i)\,d\varphi\\
&=\left[\Delta z e_z\left(i,\, k+\frac{1}{2}\right)+\rho(i)\left\{e_\varphi(i,\, k)-e_\varphi(i,\, k+1)\right\}\right]\\
&\quad\cdot\left\{\sin\varphi(j+1)-\sin\varphi(j)\right\}.
\end{aligned} \tag{3}$$

The surface integral of magnetic flux density is approximately given by

$$\begin{aligned}
&\mu\iint_H ds\\
&\simeq\frac{\mu(i,\, k+1)+\mu(i+1,\, k+1)}{2}\Delta z\\
&\quad\cdot\int_{\varphi(j)}^{\varphi(j+1)} h_\rho\left(i, k+\frac{1}{2}\right)\cos\varphi\rho(i)\,d\varphi\\
&=\frac{\mu(i,\, k+1)+\mu(i+1,\, k+1)}{2}\Delta z\rho(i)h_\rho\left(i, k+\frac{1}{2}\right)\\
&\quad\cdot\left\{\sin\varphi(j+1)-\sin\varphi(j)\right\}.
\end{aligned} \tag{4}$$

Substituting these two equations and writing a central difference expression at time step n to replace the time derivative, we obtain

$$\begin{aligned}
&h_\rho^{n+(1/2)}\left(i, k+\frac{1}{2}\right)\\
&\quad=h_\rho^{n-(1/2)}\left(i, k+\frac{1}{2}\right)\\
&\qquad-\frac{2\Delta t}{\left\{\mu(i,\, k+1)+\mu(i+1,\, k+1)\right\}\Delta z\rho(i)}\\
&\qquad\cdot\left[\Delta z e_z^n\left(i, k+\frac{1}{2}\right)+\rho(i)\left\{e_\varphi^n(i,\, k)-e_\varphi^n(i,\, k+1)\right\}\right]
\end{aligned} \tag{5}$$

where Δt is the time increment. Applying Faraday's Law on the $z-\rho$ and $\rho-\varphi$ faces of the cell, we obtain

$$\begin{aligned}
&h_\varphi^{n+(1/2)}\left(i+\frac{1}{2}, k+\frac{1}{2}\right)\\
&\quad=h_\varphi^{n-(1/2)}\left(i+\frac{1}{2}, k+\frac{1}{2}\right)-\frac{\Delta t}{\mu(i+1,\, k+1)\Delta\rho\Delta z}\\
&\qquad\cdot\left[\Delta\rho\left\{e_\rho^n\left(i+\frac{1}{2}, k+1\right)-e_\rho^n\left(i+\frac{1}{2}, k\right)\right\}\right.\\
&\qquad\left.+\Delta z\left\{e_z^n\left(i, k+\frac{1}{2}\right)-e_z^n\left(i+1, k+\frac{1}{2}\right)\right\}\right]
\end{aligned} \tag{6}$$

$$h_z^{n+(1/2)}\left(i+\frac{1}{2},\,k\right) = h_z^{n-(1/2)}\left(i+\frac{1}{2},\,k\right) + \frac{4\Delta t}{\{\mu(i,\,k+1)+\mu(i+1,\,k+1)\}\{\rho^2(i+1)-\rho^2(i)\}} \cdot\left\{\Delta\rho e_\rho^n\left(i+\frac{1}{2},\,k\right)-\rho(i+1)e_\varphi^n(i+1,\,k) + \rho(i)e_\varphi^n(i,\,k)\right\}. \tag{7}$$

Next, we consider an electric field on a side and the four magnetic fields on the faces sharing the side. Applying Ampere's Law to these fields, we obtain the following equations for computing the electric fields:

$$e_\rho^{n+1}\left(i+\frac{1}{2},\,k\right) = e_\rho^n\left(i+\frac{1}{2},\,k\right) - \frac{\Delta t}{\varepsilon_\rho}\left[\Delta z h_z^{n+1/2}\left(i+\frac{1}{2},\,k\right)+\left\{\rho(i)+\frac{1}{2}\Delta\rho\right\} \cdot\left\{h_\varphi^{n+1/2}\left(i+\frac{1}{2},\,k+\frac{1}{2}\right)-h_\varphi^{n+1/2}\left(i+\frac{1}{2},\,k-\frac{1}{2}\right)\right\}\right] \tag{8}$$

$$e_\varphi^{n+1}(i,\,k) = e_\varphi^n(i,\,k) + \frac{\Delta t}{\varepsilon_\varphi}\left[\Delta z\left\{h_z^{n+1/2}\left(i-\frac{1}{2},\,k\right)-h_z^{n+1/2}\left(i+\frac{1}{2},\,k\right)\right\} + \Delta\rho\left\{h_\rho^{n+1/2}\left(i,\,k+\frac{1}{2}\right)-h_\rho^{n+1/2}\left(i,\,k-\frac{1}{2}\right)\right\}\right] \tag{9}$$

$$e_z^{n+1}\left(i,\,k+\frac{1}{2}\right) = e_z^n\left(i,\,k+\frac{1}{2}\right) + \frac{\Delta t}{\varepsilon_z}\left[\Delta\rho h_\rho^{n+1/2}\left(i,\,k+\frac{1}{2}\right) +\left\{\rho(i)+\frac{1}{2}\Delta\rho\right\}h_\varphi^{n+1/2}\left(i+\frac{1}{2},\,k+\frac{1}{2}\right) - \left\{\rho(i)-\frac{1}{2}\Delta\rho\right\}h_\varphi^{n+1/2}\left(i-\frac{1}{2},\,k+\frac{1}{2}\right)\right] \tag{10}$$

where

$$\varepsilon_\rho = \frac{\Delta z}{2}\left\{\varepsilon(i+1,\,k)+\varepsilon(i+1,\,k+1)\right\}\left\{\rho(i)+\frac{1}{2}\Delta\rho\right\} \tag{11}$$

$$\varepsilon_\varphi = \frac{1}{4}\Delta\rho\Delta z\{\varepsilon(i,\,k)+\varepsilon(i,\,k+1)+\varepsilon(i+1,\,k) +\varepsilon(i+1,\,k+1)\} \tag{12}$$

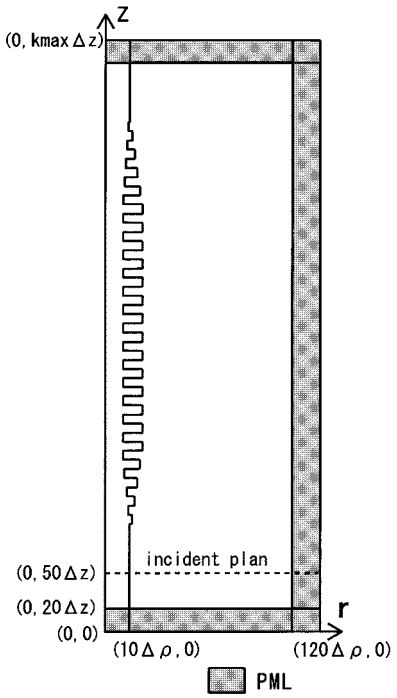

Fig. 3. Zoning of the computational region. The shape of the waveguide is also depicted near $\rho = 10\Delta\rho$ in the region.

$$\varepsilon_z = \frac{\varepsilon(i,\,k+1)}{2}\left\{\rho(i)\Delta\rho-\frac{1}{4}\Delta\rho^2\right\} + \frac{\varepsilon(i+1,\,k+1)}{2}\left\{\rho(i+1)\Delta\rho-\frac{1}{4}\Delta\rho^2\right\}. \tag{13}$$

The equations for computing the fields of the on-z-axis cell can be deduced by taking account of the parity about the axis. For the sake of space limitation, they are not given here. These equations at both off-z-axis cells and on-z-axis cells are independent of φ so that all we have to calculate are $e_\rho(i+1/2,\,k)$, $e_\varphi(i,\,k)$, $e_z(i,\,k+1/2)$, $h_\rho(i,\,k+1/2)$, $h_\varphi(i+1/2,\,k+1/2)$, and $h_z(i+1/2,\,k)$ $(i=0,\,1,\,2,\,\ldots,i_{\max},\,k=0,\,1,\,2,\,\ldots,k_{\max})$.

Fig. 3 shows zoning of the computational region. The one side coincides with the z-axis, and the other three sides are surrounded by perfect matched layers (PMLs). HE_{11} wave field incident to the waveguide is generated on the plane $k=50$. The total fields are calculated in the region $50 < k \le k_{\max}-20$, and the scattered fields are calculated in the region $20 \le k \le 50$. In view of wavelength, the lattice space increments $\Delta\rho$ and Δz are chosen as $\Delta\rho,\,\Delta z = 0.1a$.

III. Analysis Results

We analyze two kinds of periodic waveguides. One is a deeply corrugated waveguide with $w_b = 0.7a$, $w_n = 0.7a$, $\rho_b = 1.5a$, and $\rho_n = 0.5a$ with $\varepsilon_r = 2.0$ and the other is the dielectric disks located in a line, which corresponds to the corrugation with $w_b = 0.7a$, $w_n = 0.7a$, $\rho_b = 2.0a$, and $\rho_n = 0.0a$. The dielectric disks located in a line can be considered an ultimate shape of corrugated rod.

A. Transducer

Uniform waveguides are connected to the periodic waveguide through transducers so that the energy of the modes is con-

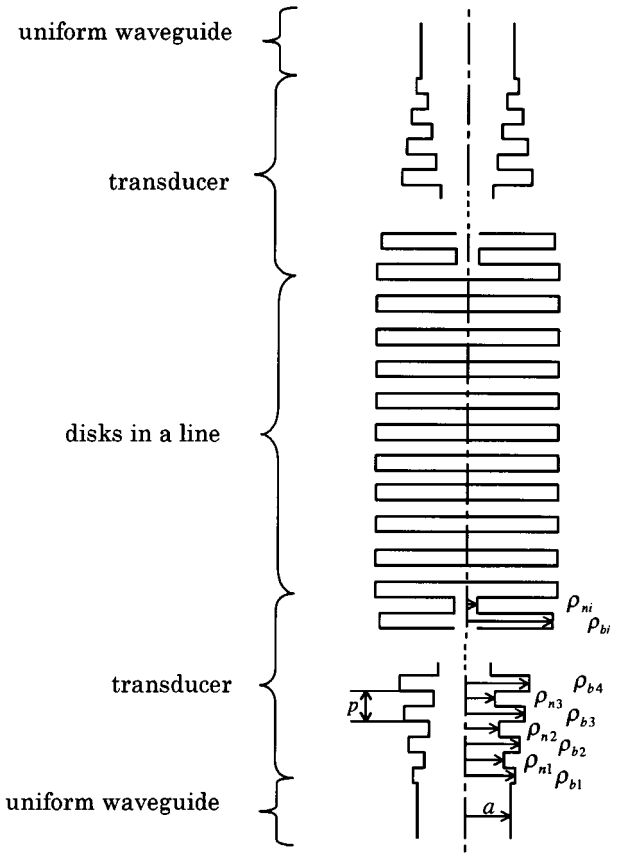

Fig. 4. Shape of the transducer between a uniform waveguide and the dielectric disks located in a line.

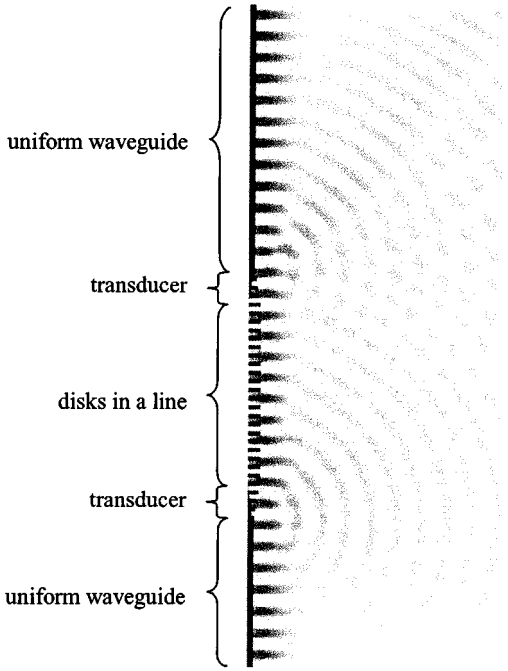

Fig. 5. Field distribution of e_z near 20 disks with $w_b = 0.7a$, $\rho_b = 2.0a$, and $p = 1.4a$ for $ka = 1.65$. The larger the field is, the darker the shade. The shades along the left-hand-side end show the cross section of disks, transducers, and uniform waveguides.

verted efficiently. Fig. 4 shows a shape of the transducer. Fig. 5 shows the field e_z of 20 disks with $w_b = 0.7a$, $\rho_b = 2.0a$, and $p = 1.4a$ for $ka = 1.65$, where the radii of the transducer are given by $\rho_{b1} = 1.1a$, $\rho_{b2} = 1.3a$, $\rho_{b3} = 1.5a$, $\rho_{b4} = 1.7a$, $\rho_{b5} = 1.9a$, $\rho_{n1} = 0.8a$, $\rho_{n2} = 0.6a$, $\rho_{n3} = 0.4a$, and $\rho_{n4} = 0.2a$. After transforming the quantities into logarithm, the instantaneous field e_z are plotted by changing brightness. The waves are radiated from two transducers. Two waves cancel each other so that hyperbolic interference fringes are observed. The loss between two uniform waveguides is 0.3 dB. The loss is caused by radiation from the transducers, as shown in Fig. 5, and reflection. Without the transducers, the loss increases to 2.1 dB. The loss can be lowered under 0.04 dB through longer transducers with $\rho_{b1} = 1.1a$, $\rho_{b2} = 1.2a$, $\rho_{b3} = 1.3a$, $\rho_{b4} = 1.4a$, $\rho_{b5} = 1.5a$, $\rho_{b6} = 1.6a$, $\rho_{b7} = 1.7a$, $\rho_{b8} = 1.8a$, $\rho_{b9} = 1.9a$, $\rho_{n1} = 0.9a$, $\rho_{n2} = 0.8a$, $\rho_{n3} = 0.7a$, $\rho_{n4} = 0.6a$, $\rho_{n5} = 0.5a$, $\rho_{n6} = 0.4a$, $\rho_{n7} = 0.3a$, $\rho_{n8} = 0.2a$, and $\rho_{n9} = 0.1a$. The converted wave is propagated along the line of disks without loss. It can be said that the line of disks operates as a lossless waveguide, except for attenuation regions discussed later.

B. Phase Constant

The spectrum in a periodic waveguide with infinite length is distributed according to the well-known relation [12]

$$\beta_q = \beta + \frac{2\pi q}{p}, \qquad q = 0, \pm 1, \pm 2, \ldots \tag{14}$$

where β denotes the phase constant of the fundamental wave. Though waveguides with infinite length do not actually exist, the propagation constant is also useful in the applications. Here, β and the attenuation constant α are presumed from the analysis data of the periodic waveguide with finite length. Through the transducer, the wave energy is converted and becomes the eigenmode of the periodic waveguide at the point above several waves apart from it. Fig. 6 shows the spatial spectrum distribution of $e_\rho(0.3a, z)$ in the deeply corrugated waveguide for $ka = 1.65$. The distribution has been obtained by discrete Fourier transforming the field data covering 36 periods. Peaks of the spectrum seems to be distributed according to (14). However, magnifying the spectrum in the direction of the horizontal axis, each peak is composed of discrete values apart from the resolution $2\pi/(14\Delta z \times 36)$. In DFT, discrete fields $f(k\Delta z)$ $(k = k_0, k_1, k_2, \ldots, k_{N-1})$ are transformed to

$$F_m = \sum_{k=k_0}^{k_{N-1}} f(k\Delta z) \exp\left\{-j\frac{2\pi}{N}(k-k_0)m\right\}, \qquad m = 0, 1, 2, \ldots, N-1. \tag{15}$$

The resolution is given by $2\pi/N\Delta z$. If $N\Delta z$ is equal to a period of the wave field, the periodic field consists of the waves with wavenumber $2\pi/(N\Delta z)m$. However, $N\Delta z$ cannot necessarily be equal to the period because the propagation constant is unknown and the field is composed of so many waves, as shown in (14). If there is a wave component not equal to $2\pi/(N\Delta z)m$, several coefficients in the neighborhood of the wave component then takes a value of nonzero. Whichever wavenumber we may choose as β, the value contains the error of order of the resolution. For increasing N, the resolution becomes high. For example, field data extending 100 wavelength is necessary for obtaining resolution accuracy better than 1%. It takes a lot of time and memory to calculate such a long region, though we have removed the dependency on the φ-direction from FDTD calculation in the previous section.

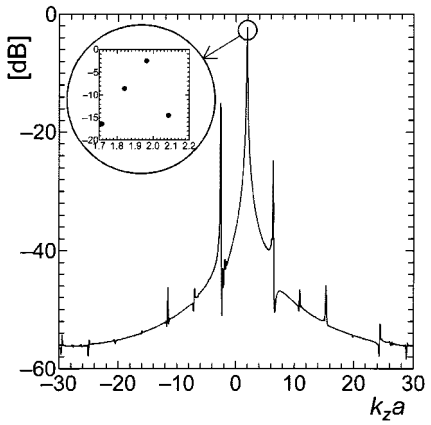

Fig. 6. DFT spectrum of the deeply corrugated waveguide with $w_b = 0.7a$, $w_n = 0.7a$, $\rho_b = 1.5a$, $\rho_n = 0.5a$, $\varepsilon_r = 2.0$, and length of 36 periods for $ka = 1.65$.

Now we are concerned with only one wave and want to determine the wavenumber, i.e., β. We intend to make $N\Delta z$ correspond not to the period of the total field, but to an integral multiple of the period of the concerned wave. Using field data at N points, $F_m(N)$ $(m = 0, 1, 2, \ldots, N-1)$ are calculated. The largest coefficient $F_{\tilde{m}(0)}(N)$ is chosen from the coefficients in the range of the fundamental wave. Similarly, using field data at $N-\ell$ $(\ell = 1, 2, \ldots, L-1)$ points, $F_m(N-\ell)$ $(m = 0, 1, 2, \ldots, N-\ell-1)$ are calculated and the largest coefficients $F_{\tilde{m}(\ell)}(N-\ell)$ are chosen, respectively. It can be expected that one of $(N-\ell)\Delta z$ $(\ell = 0, 1, 2, \ldots, L-1)$ is close to an integral multiple of the period of the concerned wave, and the $F_{\tilde{m}(\ell)}(N-\ell)$ then becomes maximum with respect to ℓ. When $F_{\tilde{m}(\ell)}(N-\ell)$ becomes maximum for $\ell = \ell_{\max}$, the estimated value for β is given by $2\pi/((N-\ell_{\max})\Delta z)\tilde{m}(\ell_{\max})$. In order to examine the validity, we apply this procedure to the field in a uniform waveguide with no corrugation and compare the results with the true value obtained analytically. In Fig. 7(a)–(d), the convergence of the estimated $\beta_{\text{uni}}a$ is plotted as a function of N for a uniform waveguide with radius a and $ka = 2.42$, where β_{uni} denotes the phase constant. L is chosen as 40, 60, 80, and 100, respectively. For $N \geq 400$ and $L \geq 80$, the estimated values converge to 2.813. Compared with the resolution 0.125 of DFT for $N = 500$, the estimated value is almost equal to the true value of 2.806.

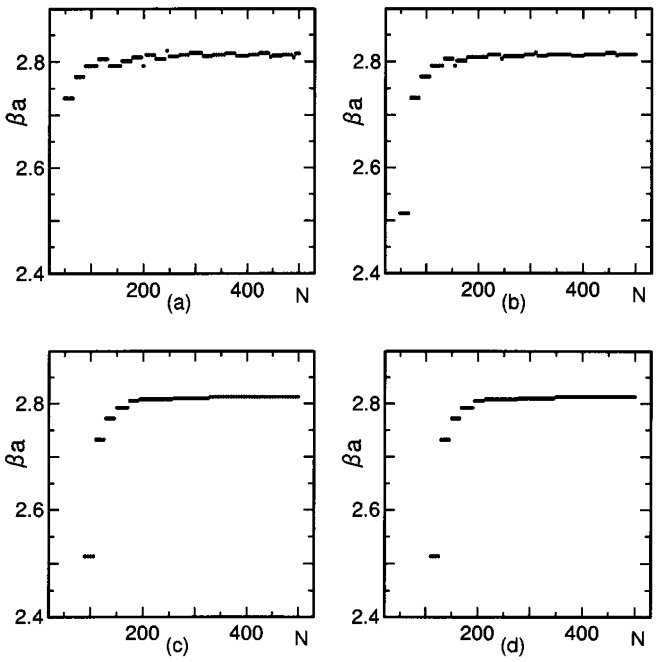

Fig. 7. Plot of the estimated βa of a uniform waveguide as increasing N for: (a) $L = 40$, (b) $L = 60$, (c) $L = 80$, (d) $L = 100$ with radius a, $\varepsilon_r = 2.0$, and $ka = 2.42$.

C. Attenuation Constant

There are attenuation regions proper to dielectric waveguides with periodic structure. The guided wave is attenuated owing to the Bragg reflection or the leaky wave. In the leaky-wave region, the guided power decreases as the wave propagates in the waveguide, and the attenuation constant can be determined by evaluating Poynting vectors passing cross sections of the waveguide. In the Bragg reflection region, on the other hand, there is a forward and backward wave. The schematic power distribution of the two waves is shown in Fig. 8, where the reflection at the transducer is neglected. The corrugation section is terminated at the right-hand-side end by a PML. In the periodic waveguide section, the forwarding wave decreases with respect to the z-direction. The reflecting wave is zero at the right-hand-side end and increases with respect to the $-z$-direction. As shown in this

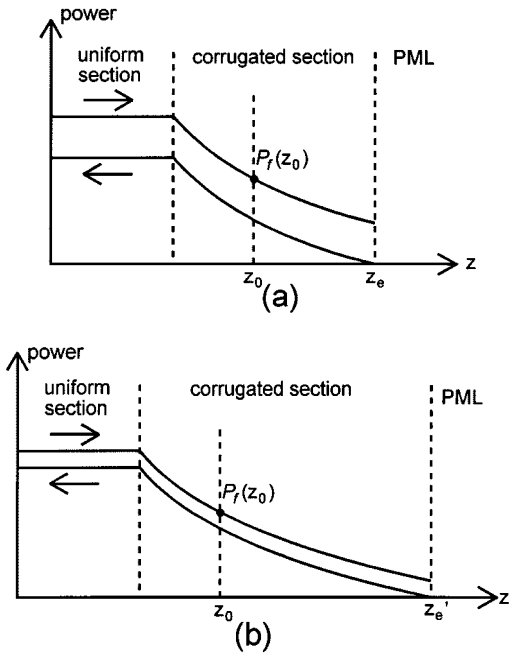

Fig. 8. Schematic power distributions of the forward and the backward waves: (a) in the shorter corrugated section and (b) in the longer corrugated section.

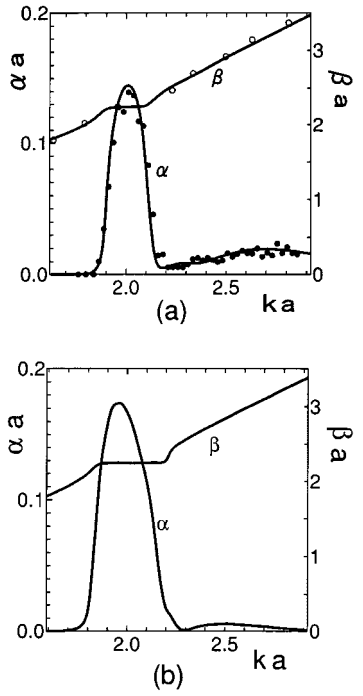

Fig. 9. Attenuation and phase constants as a function of ka for: (a) the deeply corrugated waveguide with $w_b = 0.7a$, $w_n = 0.7a$, $\rho_b = 1.5a$, $\rho_n = 0.5a$, and $\varepsilon_r = 2.0$ and (b) the disk waveguide with $w_b = 0.7a$, $w_n = 0.7a$, $\rho_b = 2.0a$, $\rho_n = 0.0a$, and $\varepsilon_r = 2.0$. The analysis results are plotted by solid lines and the experimental results are plotted by circles.

figure, the Poynting vector is constant on any cross sections. In Fig. 8(a), the Poynting vector on the plane $z = z_0$ is given by

$$\mathbf{Po}(z_0) = \exp\{-2\alpha(z_e - z_0)\}P_f(z_0)\hat{z} \tag{16}$$

where $P_f(z_0)\hat{z}$ denotes the Poynting vector of the forwarding wave on the plane $z = z_0$. Fig. 8(b) shows the power distribution in a longer corrugated section. The Poynting vector on the plane $z = z_0$ is given by

$$\mathbf{Po}'(z_0) = \exp\{-2\alpha(z_e' - z_0)\}P_f(z_0)\hat{z}. \tag{17}$$

Thus, the attenuation constant α is given by

$$\alpha = \frac{\ln Po(z_0) - \ln Po'(z_0)}{2(z_e' - z_e)}. \tag{18}$$

The dispersion relations of the deeply corrugated and disk waveguides are shown in Fig. 9(a) and (b), respectively. The disk waveguide also has the propagation region without loss in the low-frequency region. Around $ka = 2.0$, α becomes large. The stopband is due to the Bragg reflection, where β is nearly equal to π/p. The field becomes very small as it propagates. After compensating the attenuation, we apply DFT to the field data and determine the estimated value of β. We measure the dispersion relations for the deeply corrugated waveguide. In Fig. 9(a), the open circles show the phase constants and the closed circles show the attenuation constants. The experimental phase constants are obtained by measuring the resonant frequencies of the corrugated waveguide with large copper sheets pasted on both end faces. The experimental attenuation constants are obtained

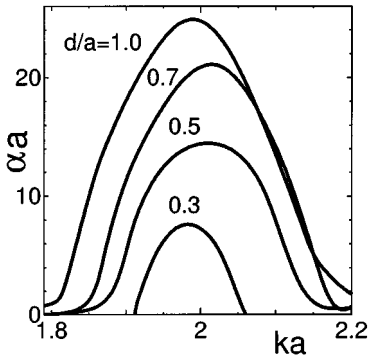

Fig. 10. Attenuation constant in the Bragg reflection region of a dielectric-rod waveguide for different corrugation depth $d = 0.3, 0.5, 0.7$, and 1.0.

by measuring the field attenuation along the corrugated waveguide. The analysis results agree comparatively with the experimental values.

Now, the HE_{11}-type wave is fed through the uniform waveguide into the periodic waveguide. Owing to the corrugation, the wave energy can be converted, in the high-frequency region, into the higher order waves with the same field distribution in the φ-direction. Higher order waves with different field distributions do not occur because the corrugation is axially symmetric. Thus, the formulation in the preceding section can be applied to the analysis of these waves with distribution in the form of $\cos\varphi$ or $\sin\varphi$. By discrete Fourier transforming the results, the spectrum of the field in the periodic waveguide can be obtained. In the low-frequency region, only the spatial spectrum relative to the wave shown in Fig. 9 appears. Above $ka = 2.90$, other peaks are found in the spectrum of field in the disk waveguide. Above $ka = 3.29$, other peaks are found in the spectrum of field in the deeply corrugated waveguide. Thus, below these frequencies, these waveguides can operate without the influence of higher order waves.

In Fig. 10, the attenuation constant in the Bragg reflection region is shown for different corrugation depth d. d is given by

$$d = \rho_b - a = a - \rho_n \tag{19}$$

so that the average radius of the waveguides may be kept constant. For increasing d, the value of attenuation increases and the stopband width becomes broader. The attenuation and stopband width of the disk waveguide are over twice as large compared with those of the waveguide with shallow corrugation $d = 0.3$.

The attenuation observed for $ka > 2.2$ or 2.3 in Fig. 9 is due to the radiative leakage. The attenuation of the disk waveguide is smaller than that of the deeply corrugated waveguide. In Fig. 11, the attenuation constant due to the radiative leakage is plotted as a function of the corrugation depth d. α takes a maximum value with respect to the corrugation depth. The amount of radiative leakage is not so large in the disk waveguide. The radiative leakage can be considered as the coupling between the guided and radiative waves. The coupling may be weak in very deep corrugation.

Fig. 12 shows the influence of the corrugation on the phase constant β outside the Bragg reflection region. The change from β_{uni} are plotted in ordinate and the corrugation depth in abscissa. Below the reflection region, for increasing d, β becomes

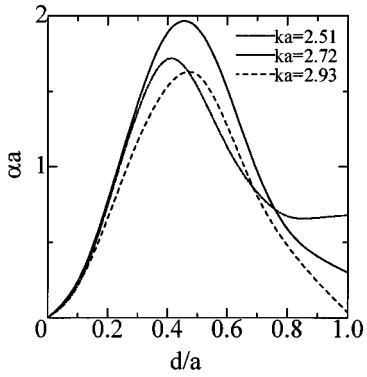

Fig. 11. Attenuation constant as a function of ka for the corrugated waveguide with $w_b = 0.7a$, $w_n = 0.7a$, and $\varepsilon_r = 2.0$.

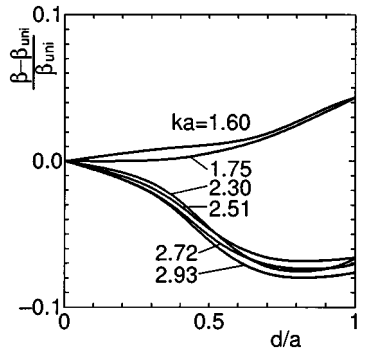

Fig. 12. Change of phase constant from $\beta_{\rm uni}$ versus corrugation depth d of a dielectric-rod waveguide with $\varepsilon_r = 2.0$.

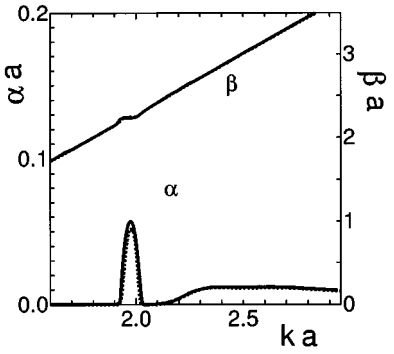

Fig. 13. Comparison of the attenuation constant and the phase constant calculated by the present method (solid line) and the Yasuura's method [11], [13] (broken line) as a function of ka for the sinusoidally corrugated waveguide.

large monotonously. Above the reflection region, for increasing d, β becomes small and has the minimum value in the very deep corrugation.

Finally, we compare the result with that of other theoretical method. Fig. 13 shows the dispersion relations of the rod waveguide with shallow sinusoidal corrugation by the present method (solid line) and the Yasuura's method [11], [13] (broken line). The surface radius is given by

$$\rho = a\left(1 + 0.3\sin\frac{2\pi z}{1.4a}\right). \tag{20}$$

Two results are almost the same. This shows the validity of the present method for corrugated waveguides.

IV. Conclusion

We have analyzed dielectric waveguides with a deep corrugation by the FDTD method. By taking account of the field distribution, we have had the FDTD formulation independent of the coordinate φ to calculate long waveguides. A procedure of deciding the propagation constant from FDTD results has been presented and the convergence of the estimated value has been confirmed. The dispersion relations has been obtained and the dependence of the amount of radiation on the corrugation amplitude has been brought out. The amount of radiative leakage takes a maximum value by choosing the corrugation amplitude properly. Dielectric disks located in a line function as a waveguide with low loss if the eigenmode is excited through the transducer. In the Bragg reflection region, the disk waveguides shows the strong attenuation characteristics with wide bandwidth. The amount of radiative leakage is not so large as that of deeply corrugated waveguides. The Bragg reflection in the corrugated rod waveguides has been recently applied to band rejection filters. The above results show that band rejection filters with large attenuation in the stopband and lower loss in the passband can be realized by using disk waveguides.

References

[1] K. O. Hill, Y. Fujii, D. C. Johnson, and B. S. Kawasaki, "Photosensitivity in optical fiber waveguides: Application to reflection filter fabrication," *Appl. Phys. Lett.*, vol. 32, no. 10, pp. 647–649, May 1978.

[2] C. C. Ghizoni, B. Chen, and C. L. Tang, "Theory and experiments on grating couplers for thin-film waveguides," *IEEE J. Quantum Electron.*, vol. QE-12, pp. 69–73, Feb. 1976.

[3] T. Itoh, "Application of gratings in a dielectric waveguide for leaky-wave antennas and band-reject filters," *IEEE Trans. Microwave Theory Tech.*, vol. MTT-25, pp. 1134–1138, Dec. 1977.

[4] S. T. Peng, T. Tamir, and H. L. Bertoni, "Theory of periodic dielectric waveguides," *IEEE Trans. Microwave Theory Tech.*, vol. MTT-23, pp. 123–133, Jan. 1975.

[5] S. L. Chuang and J. A. Kong, "Wave scattering and guidance by dielectric waveguides with periodic surfaces," *J. Opt. Soc. Amer.*, vol. 73, no. 5, pp. 669–679, May 1983.

[6] S. Sandstrom, "Stopbands in a corrugated parallel plate waveguide," *J. Acoust. Soc. Amer.*, vol. 79, no. 5, pp. 1293–1298, May 1986.

[7] K. O. Ogawa, W. S. C. Chang, B. L. Sopori, and F. J. Rosenbaum, "A theoretical analysis of etched grating couplers for integrated optics," *IEEE J. Quantum Electron.*, vol. QE-9, pp. 29–42, Jan. 1973.

[8] D. Marcuse and R. Derosier, "Mode conversion caused by diameter changes of a round dielectric waveguide," *Bell Syst. Tech. J.*, vol. 48, pp. 3216–3233, Oct. 1969.

[9] M. T. Wlodarczyk and S. R. Seshadri, "Excitation and scattering of guided modes on a dielectric cylinder with a periodically varying radius," *J. Appl. Phys.*, vol. 57, no. 3, pp. 943–955, Feb. 1985.

[10] S. L. Lundqvist, "A penetrable dielectric waveguide with periodically varying circular cross section," *IEEE Trans. Microwave Theory Tech.*, vol. MTT-35, pp. 282–287, Mar. 1987.

[11] K. Yasumoto and H. Kubo, "Numerical analysis of cylindrical dielectric waveguide with a periodically varying circular cross section," *J. Opt. Soc. Amer. A, Opt. Image Sci.*, vol. 7, no. 11, pp. 2069–2074, Nov. 1990.

[12] C. Elachi, "Waves in active and passive periodic structures: A review," *Proc. IEEE*, vol. 64, pp. 1666–1698, Dec. 1976.

[13] H. Kubo, "Leakage characteristics of the cylindrical dielectric waveguide with a periodically varying radius," *Microwave Opt. Technol. Lett.*, vol. 5, pp. 718–721, 1992.

Hiroshi Kubo (M'92) received the B.E., M.E., and D.E. degrees from Kyushu University, Fukuoka, Japan, in 1978, 1980, and 1993, respectively.

From 1980 to 1985, he was with the Nippon Electric Company, Tokyo, Japan, where he was engaged in the development of mobile communication system. From 1985 to 1987, he was a Development Engineer with the Kyushu Matsushita Electric Company, Fukuoka, Japan. From 1987 to 1991, he was a Research Associate with Kyushu University. Since 1991, he has been with the Department of Electrical and Electronic Engineering, Yamaguchi University, Ube, Japan, where he is currently an Associate Professor. His main research interests are radio communication networks and microwave communication devices.

Masayoshi Tahara received the B.E. and M.E. degrees from Yamaguchi University, Ube, Japan, in 1996 and 1998, respectively.

Since 1998, he has been with the Japan Radio Company, Tokyo, Japan.